EPJ manuscript No.
(will be inserted by the editor)

Measurement of the $e^+e^- \to K^+K^-\pi^0$ cross section with the SND detector

The SND Collaboration

M. N. Achasov[1,2], A. Yu. Barnyakov[1,2], M. Yu. Barnyakov[1], A. A. Baykov[1,2], K. I. Beloborodov[1,2], A. V. Berdyugin[1,2], D. E. Berkaev[1,2], A. G. Bogdanchikov[1], A. A. Botov[1], A. R. Buzykaev[1], T. V. Dimova[1,2], V. P. Druzhinin[1,2], V. B. Golubev[1], L. V. Kardapoltsev[1,2], A. G. Kharlamov[1,2], A. A. Korol[1,2], D. P. Kovrizhin[1], E. A. Kravchenko[1,2], A. S. Kupich[1], A. P. Lysenko[1], K. A. Martin[1], N. Yu. Muchnoy[1,2], N. A. Melnikova[1] A. E. Obrazovsky[1], A. P. Onuchin[1], E. V. Pakhtusova[1] E. A. Perevedentsev[1,2], K. V. Pugachev[1,2], Y. S. Savchenko[1,2], S. I. Serednyakov[1,2], P. Yu. Shatunov[1], Yu. M. Shatunov[1,2], D. A. Shtol[1], D. B. Shwartz[1,2], Z. K. Silagadze[1,2], I. K. Surin[1], Yu. A. Tikhonov[1,2], Yu. V. Usov[1], I. M. Zemlyansky[1,2], V. N. Zhabin[1], and V. V. Zhulanov[1,2]

[1] Budker Institute of Nuclear Physics, SB RAS, Novosibirsk, 630090, Russia
[2] Novosibirsk State University, Novosibirsk, 630090, Russia

arXiv:2007.04527v2 [hep-ex] 28 Dec 2020

Abstract The process $e^+e^- \to K^+K^-\pi^0$ is studied with the SND detector at the VEPP-2000 e^+e^- collider. Basing on data with an integrated luminosity of 26.4 pb^{-1} we measure the $e^+e^- \to K^+K^-\pi^0$ cross section in the center-of-mass energy range from 1.28 up to 2 GeV. The measured mass spectrum of the $K\pi$ system indicates that the dominant mechanism of this reaction is the transition through the $K^*(892)K$ intermediate state. The cross section for the $\phi\pi^0$ intermediate state is measured separately. The SND results are consistent with previous measurements in the BABAR experiment and have comparable accuracy. We study the effect of the interference between the $\phi\pi^0$ and K^*K amplitudes. It is found that the interference gives sizable contribution to the measured $e^+e^- \to \phi\pi^0 \to K^+K^-\pi^0$ cross section below 1.7 GeV.

1 Introduction

This paper is devoted to the study of the reaction $e^+e^- \to K^+K^-\pi^0$ in the experiment with the SND detector at the VEPP-2000 e^+e^- collider [1]. This reaction is one of three charge modes of the process $e^+e^- \to K\bar{K}\pi$, which gives a sizable contribution (about 12% at the center-of-mass (c.m.) energy $\sqrt{s} \approx 1.65$ GeV) to the total cross section of e^+e^- annihilation into hadrons, and is the key process for measuring the $\phi(1680)$ resonance parameters. The reaction $e^+e^- \to K^+K^-\pi^0$ was first observed in the DM2 experiment [2]. The accuracy of measuring its cross section was significantly improved in the BABAR experiment [3], in which the process $e^+e^- \to K^+K^-\pi^0$ was studied using the initial state radiation method. In Ref. [3], it is shown that the process $e^+e^- \to K^+K^-\pi^0$ proceeds through the $K^{*\pm}(892)K^\mp$, $\phi(1020)\pi^0$, and $K_2^{*\pm}(1430)K^\mp$ intermediate states. In the VEPP-2000 energy range, $\sqrt{s} < 2$ GeV, the $K_2^{*\pm}(1430)K^\mp$ contribution is expected to be small. The cross section of the process $e^+e^- \to \phi(1020)\pi^0$ was also measured in the BABAR experiment [4] in the final state $K_SK_L\pi^0$.

The aim of this work is to measure the cross section for the process $e^+e^- \to K^+K^-\pi^0$ with an accuracy comparable to that of BABAR [3].

2 Detector and experiment

The VEPP-2000 e^+e^- collider operate in the c.m. energy range from 0.32 to 2.01 GeV. SND [5] is a general-purpose non-magnetic detector. It comprises a tracking system, a particle identification system based on aerogel threshold Cherenkov counters, an electromagnetic calorimeter, and a muon system. The main part of the detector is a three-layer spherical calorimeter based on NaI (Tl) crystals with a thickness of $13.4X_0$, where X_0 is the radiation length. Its energy resolution is $\sigma_{E_\gamma}/E_\gamma = 4.2\%/\sqrt[4]{E_\gamma\ (\mathrm{GeV})}$, and the angular resolution is $\sigma_{\theta,\phi} = 0.82^\circ/\sqrt{E_\gamma(\mathrm{GeV})}$, where E_γ is the photon energy. The calorimeter covers about 95% of the solid angle.

The tracking system, which is used for measurement of directions and production points of charged particles, is located inside the calorimeter, around the collider beam pipe. It consists of a nine-layer cylindrical drift chamber and a proportional chamber with cathode strip readout. The tracking system covers a solid angle of 94% of 4π.

The charged particle identification is provided by the system of aerogel Cherenkov counters (ACC) [6]. It consists of nine counters forming a cylinder located around the tracking system. The counters cover the polar angle region $50^\circ < \theta < 132^\circ$. The aerogel radiator has a refractive index of $n = 1.13$ and a thickness of 30 mm. The

Cherenkov light is collected and transmitted to photodetectors using wavelength shifters located inside the aerogel radiator. Information from the ACC is used only if the charged particle track extrapolates to the ACC active area that excludes the regions of shifters and gaps between counters. The active area is 81% of the ACC area.

The calorimeter is surrounded by the 10 cm thick iron absorber and the muon system, which consists of a layer proportional tubes and a layer of scintillation counters with an 1 cm thick iron sheet between them.

In this work we analyze a data sample with an integrated luminosity of 26.4 pb^{-1} recorded in 2011–2012. In the energy range under study, 1.27–2.00 GeV, data were collected in 44 energy points. Because of the absence of narrow structures in the cross sections under study, these energy points are merged into 27 energy intervals. The luminosity-weighted average c.m. energies for these intervals are listed in Table 1.

For simulation of signal events, a Monte Carlo (MC) event generator is used based on formulas from Ref. [7]. It is assumed that the process $e^+e^- \to K^+K^-\pi^0$ proceeds through the $K^*(892)^\pm K^\mp$ and $\phi\pi^0$ intermediate states. The following background processes are also simulated:

$$\begin{aligned} &e^+e^- \to \pi^+\pi^-\pi^0,\ \pi^+\pi^-\pi^0\pi^0,\ \pi^+\pi^-\pi^0\pi^0\pi^0,\\ &e^+e^- \to K^+K^-,\ K_SK_L,\ K_SK^\pm\pi^\mp,\ K_LK^\pm\pi^\mp,\\ &e^+e^- \to K^+K^-\pi^0\pi^0,\ K_SK^\pm\pi^\mp\pi^0,\ K_LK^\pm\pi^\mp\pi^0. \quad (1) \end{aligned}$$

Event generators for the signal and background processes include radiation corrections [8]. The angular distribution of the extra photon emitted from the initial state is generated according to Ref. [9]. Interactions of the generated particles with the detector materials are simulated using the GEANT4 software [10]. The simulation takes into account variations of experimental conditions during data taking, in particular, dead detector channels, and beam-generated background. The beam background leads to the appearance of spurious charged tracks and photons in the events of interest. To take this effect into account, the simulation uses special background events recorded during data taking with a random trigger, which are superimposed on simulated events.

The integrated luminosity is measured on $e^+e^- \to e^+e^-$ events with an uncertainty better than 2% [11].

3 Events selection

Events from the $e^+e^- \to K^+K^-\pi^0$ process are detected as two charged particles and two photons from the π^0 decay. An event may contain additional charged tracks originating from δ electrons and beam background, and spurious photons originating from splitting of the electromagnetic shower, kaon nuclear interaction in the calorimeter, and beam background. We select events with two or three charged particles and two or more photons with energy higher than 30 MeV. The charged-particle track is required to have at least 4 hits in the drift chamber. At least two charged particles must originate from the interaction region, i.e. satisfy the conditions: $d_i < 0.3$ cm, $|z_i| < 10$ cm, $i = 1, 2$, and $|z_1 - z_2| < 5$ cm, where d_i is the distance between the track and the beams axis, and the z_i is the z-coordinate of the track point closest to the beam axis. If there are three charged particles satisfying the above criteria, two of them with the best χ^2 of the fit to a common vertex are selected. The third must have $d_3 > 0.2$ cm.

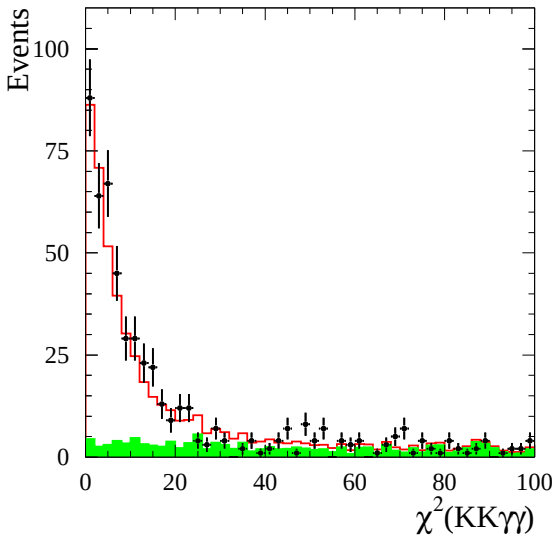


Figure 1. The $\chi^2(KK2\gamma)$ distribution for data events with $100 \le m_{\gamma\gamma} \le 170$ MeV/c^2 from the interval $1.5 < \sqrt{s} < 1.72$ GeV (points with error bars). The solid histogram is the sum of the simulated signal distribution and the background distribution. The hatched histogram represents the background.

For events passing the primary selection described above, the kinematic fit with four constraints of energy and momentum balance to the hypothesis $e^+e^- \to K^+K^-\gamma\gamma$ is performed. From the fit, we determine the kaon momenta and refine the photon energies. The quality of the fit is characterized by the parameter $\chi^2(KK2\gamma)$. If there are more than two photons in an event, all two-photon combinations are tested and one with the smallest χ^2 is selected. The $\chi^2(KK2\gamma)$ distributions for signal and background events are shown in Fig. 1. A method to obtain the background distribution is described in Sec. 6. The fitted photon parameters are used to calculate the two-photon invariant mass $m_{\gamma\gamma}$. The kinematic fits are also performed to the hypotheses $\pi^+\pi^-\gamma\gamma$ and $\pi^+\pi^-\pi^0\pi^0$, and the parameters $\chi^2(2\pi2\gamma)$ and $\chi^2(4\pi)$ are determined. The fit to the $\pi^+\pi^-\pi^0\pi^0$ hypothesis includes two additional π^0-mass constraints and is applied to events with four photons. To select the events of the process $e^+e^- \to K^+K^-\pi^0$, the following conditions are used:

$$\begin{aligned} \chi^2(KK2\gamma) &< 40,\\ \chi^2(2\pi2\gamma) &> 20,\\ \chi^2(4\pi) &> 20. \end{aligned}$$

4 Kaon identification

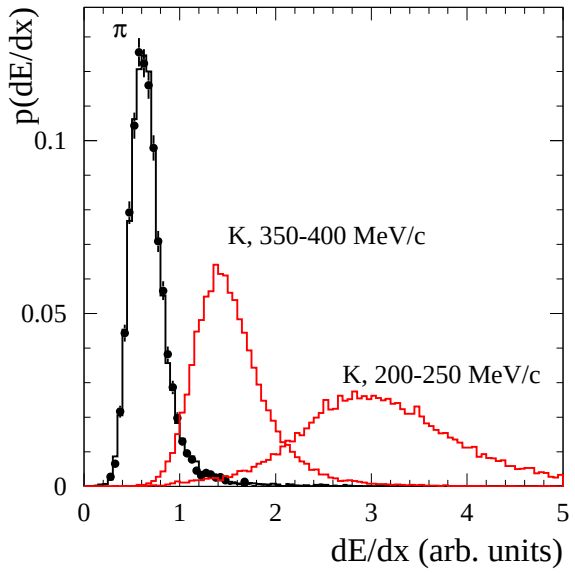


Figure 2. The probability density distribution of the ionization losses in the drift chamber for pions and kaons. The points with error bars represent the data distribution for pions from $e^+e^- \to \pi^+\pi^-\pi^0\pi^0$ events, the histogram is the same simulated distribution. The kaon distributions for two momentum ranges are obtained using $e^+e^- \to K^+K^-\pi^0$ simulation.

For kaon identification, information about ACC response and ionization losses of charged particles in the drift chamber (dE/dx) measured in e$^\pm$ dE/dx units is used.

In the energy range of VEPP-2000 charged kaons do not produce a Cherenkov signal in the ACC. For pions the threshold momentum is 265 MeV/c.

The dE/dx distribution for pions from the background process $e^+e^- \to \pi^+\pi^-\pi^0\pi^0$ is shown in Fig. 2. For kaons from the process $e^+e^- \to K^+K^-\pi^0$ in the energy range under study, momenta vary from 100 MeV/c to 800 MeV/c, and there is a strong dependence of dE/dx on the kaon momentum. It is illustrated in Fig. 2, where the kaon dE/dx distributions obtained using $e^+e^- \to K^+K^-\pi^0$ simulation is shown for two ranges of kaon momentum.

A charged particle is identified as a kaon if it passes through the active ACC area and does not produce a Cherenkov signal. If the momentum of this particle determined from the kinematic fit to the $e^+e^- \to K^+K^-\pi^0$ model is less than 300 MeV/c, the additional condition $dE/dx > 1$ is applied. We select events with one or two identified kaons. For events with one identified kaon, the second charged particle must not pass the active ACC region, have the polar angle in the range from 40° to 140°, the fitted momentum less than 450 MeV/c, and $dE/dx > 1$.

5 Background suppression

The significant background for the process under study comes from multihadron processes containing several neutral pions in the final state. To suppress this background, the condition $E_{\rm extra} < 0.3$ is used, where $E_{\rm extra}$ is the total energy of photons not included in the kinematic fit, normalized to the beam energy $\sqrt{s}/2$. The $E_{\rm extra}$ distributions for selected data events, signal simulation, and simulation of the background processes (1) are shown in Fig. 3, for $\sqrt{s} > 1.8$ GeV, where the effect of the cut on $E_{\rm extra}$ is maximal. The contributions of different background processes to the background spectrum are calculated using their measured cross sections.

For additional suppression of background, the conditions on the minimum ($P_{\rm min}$) and maximum ($P_{\rm max}$) kaon momenta in an event obtained from the kinematic fit to the $e^+e^- \to K^+K^-\gamma\gamma$ hypothesis are used. The minimum kaon momentum is required to be larger than 100 MeV/c, while the cut on the maximum momentum depends on c.m. energy and is chosen such that the fraction rejected signal events does not exceed 10%. Figure 4 shows the $P_{\rm max}$ distribution for selected data events at $\sqrt{s} = 1.89$ GeV, and the simulated distributions for the process under study and background processes. At this energy, $P_{\rm max} > 500$ MeV/c is required.

To suppress the background from collinear events of the processes $e^+e^- \to e^+e^-$, $\pi^+\pi^-$, K^+K^-, we reject events with $|\Delta\varphi| < 5°$ and $|\Delta\theta| < 5°$, where $\Delta\varphi = |\varphi_1 - \varphi_2| - 180°$, $\Delta\theta = \theta_1 + \theta_2 - 180°$, and φ_i and θ_i are the azimuthal and polar angles of the charged particles, respectively.

The process $e^+e^- \to \phi\pi^0$ will be analyzed separately in Sec. 9. When studying the $e^+e^- \to K^+K^-\pi^0$ process, the $\phi\pi^0$ events are removed by the condition $m_{\rm rec} > 1.05$ GeV/c^2, where m_{rec} is the mass recoiling against the photon pair calculated after the kinematic fit to the $e^+e^- \to K^+K^-\gamma\gamma$ hypothesis.

The two-photon invariant mass spectrum for selected data events from the energy range $\sqrt{s} = 1.50$–1.72 GeV, where the $e^+e^- \to K^+K^-\pi^0$ cross section is maximal, is shown in Fig. 5. This spectrum in the mass range $30 < m_{\gamma\gamma} < 250$ MeV/c^2 is fitted by a sum of signal and background distributions. The signal distribution is obtained using the $e^+e^- \to K^+K^-\pi^0$ simulation. The background distribution is a sum of the simulated mass spectrum for the processes (1) and a linear function describing contribution of other background processes. The simulated background spectrum is multiplied by the scale factor $\alpha_{\rm b}$. During the fit, $\alpha_{\rm b}$ is varied within 10% around unity. The fit result is shown in Fig. 5 by the solid histogram. The dashed histogram represents the total fitted background. The hatched histogram shows the part of the background described by the linear function. It is seen that the background processes (1) describe approximately 80% of the background observed in data.

To estimate the systematic uncertainty in the number of signal events due to incorrect description of the background shape, the fit with free $\alpha_{\rm b}$ is performed. The difference between the results of the two fits is taken as

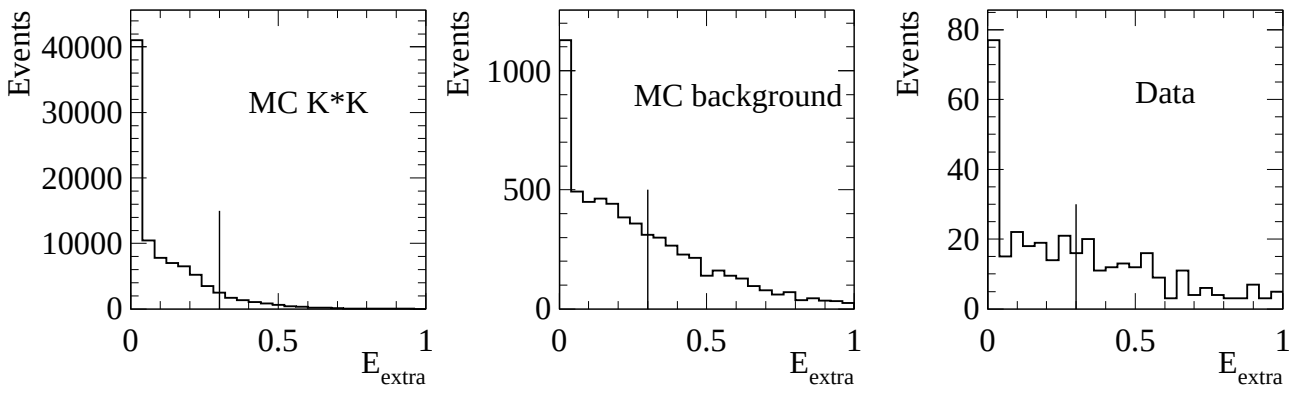


Figure 3. The $E_{\rm extra}$ distribution for data events with $\sqrt{s} > 1.8$ GeV and simulated events of the process under study and background processes. The vertical line indicates the boundary of the condition $E_{\rm extra} < 0.3$.

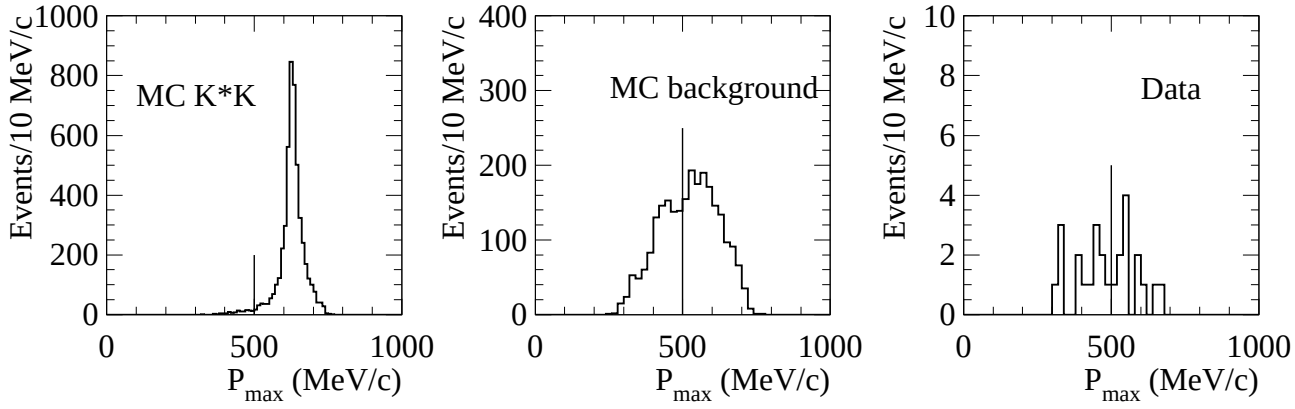


Figure 4. The $P_{\rm max}$ distribution for selected data events and simulated events of the process under study and background processes at $\sqrt{s} = 1.89$ GeV. The vertical line indicates the boundary of the condition $P_{\rm max} > 500$ MeV/c.

a measure of systematic uncertainty. The fitted numbers of $e^+e^- \to K^+K^-\pi^0$ events with the statistical and systematic uncertainties for different energy points are listed in Table 1. In the energy range $\sqrt{s} = 1.45$–1.70 GeV the systematic uncertainty is about 5%.

6 Detection efficiency

The visible cross for the process under study $\sigma_{{\rm vis},i} = N_i/L_i$, where N_i and L_i are the number of selected events and the integrated luminosity for the $i-$th energy point, is related to the Born cross section σ_0 by the following expression:

$$\sigma_{\rm vis}(\sqrt{s}) = \int\limits_0^{z_{\rm max}} dz \sigma_0(\sqrt{s(1-z)}) F(z,s) \varepsilon(\sqrt{s},z), \quad (2)$$

where $F(z,s)$ is a function describing the probability of emission of photons with the energy $z\sqrt{s}/2$ from the initial state [8], $\varepsilon(\sqrt{s},z)$ is the detection efficiency, $z_{\rm max} = 1 - (m_{\pi^0}+2m_K)^2/s$, m_{π^0} and m_K are the π^0 and $K^\pm$ masses, respectively.

The detection efficiency for $e^+e^- \to K^+K^-\pi^0$ events is determined using MC simulation as a function of $\sqrt{s}$ and z. The dependence of the efficiency on z at $\sqrt{s} = 1.575$ GeV is shown in Fig. 6. The values of the efficiency at zero photon energy $\varepsilon_0(\sqrt{s}) = \varepsilon(\sqrt{s},0)$ for different energy points are listed in Table 1.

Inaccuracy in simulation of distributions of parameters used in event selection leads to a systematic uncertainty in the detection efficiency determined using the simulation. The most critical selection parameters are $\chi^2(KK\gamma\gamma)$, dE/dx, and $E_{\rm extra}$. To estimate the systematic uncertainty, we use events from the energy region $1.5 < \sqrt{s} < 1.72$ GeV, where the $e^+e^- \to K^+K^-\pi^0$ cross section is maximal, change the selection conditions, and study the change in the measured signal cross section. For the parameters mentioned above, the loosened selection criteria $\chi^2(KK\gamma\gamma) < 80$, $dE/dx > 0.8$, and $E_{\rm extra} < 0.5$ are used instead of

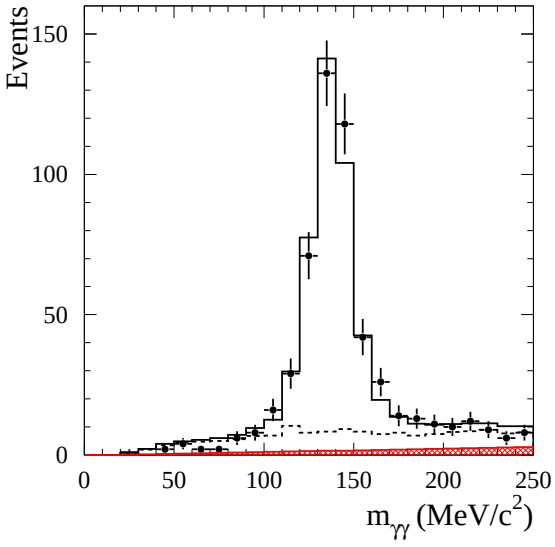


Figure 5. The two-photon invariant mass spectrum for selected data events with $\sqrt{s}$ = 1.5–1.72 GeV (points with errors). The solid histogram is the result of the fit to the data spectrum with the sum of the signal and background distributions. The dashed histogram represents the fitted background. The hatched histogram shows the part of the background described by the linear function.

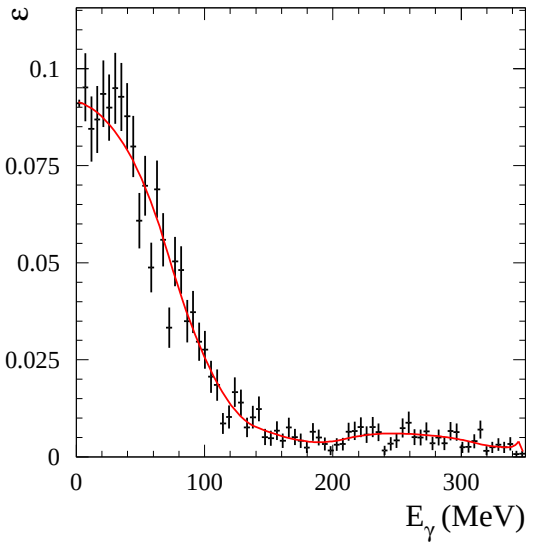


Figure 6. The dependence of the detection efficiency for $e^+e^- \to K^+K^-\pi^0$ events at $\sqrt{s} = 1.575$ GeV on the energy of the photon emitted from the initial state. The dependence is approximated by a smooth function.

the standard criteria $\chi^2(KK\gamma\gamma) < 40$, $dE/dx > 1$, and $E_{\rm extra} < 0.3$. It is found that the total systematic uncertainty due to these conditions does not exceed 8%.

Figure 1 shows the $\chi^2(KK2\gamma)$ distribution for data events with $100 \le m_{\gamma\gamma} \le 170$ MeV/c^2 from the interval $1.5 < \sqrt{s} < 1.72$ GeV. It is seen that the data distribution is in good agreement with the sum of the simulated signal distribution and the background distribution. The latter is a sum of the simulated distribution for the background processes (1) and the distribution for unaccounted background, which fraction is about 20% (see Sec. 5). We assume that this unaccounted background has a linear shape of the $m_{\gamma\gamma}$ spectrum and therefore can be estimated in each χ^2 bin using the equation $N_{lin} = (N_2 - r_s N_1)/(2 - r_s)$, where N_1 and N_2 are the numbers of selected data events with subtracted background from the processes (1) in the signal region ($100 < m_{\gamma\gamma} < 170$ MeV/c^2) and the sidebands ($30 < m_{\gamma\gamma} < 100$ MeV/c^2 and $170 < m_{\gamma\gamma} < 240$ MeV/c^2), respectively, and r_s is the N_2/N_1 ratio for signal events obtained using simulation.

Other sources of the systematic uncertainty on the detection efficiency were studied in Ref. [12]. These are the uncertainties associated with the kaon identification using the ACC (1.2%), the definition of the ACC active region (0.3%), the inaccuracy in simulation of kaons nuclear interaction (0.1%), and the photon conversion in material before the tracking system (0.7%). The total systematic uncertainty on the detection efficiency is 8%.

7 Study of the $K^\pm\pi^0$ invariant mass spectrum

It is shown in Ref. [3] that the process $e^+e^- \to K^+K^-\pi^0$ proceeds through the $K^{*\pm}(892)K^\mp$ and $K_2^{*\pm}(1430)K^\mp$ intermediate states. In the VEPP-2000 energy range, below 2 GeV, the dominant intermediate state is expected to be $K^{*\pm}(892)K^\mp$. Figure 7 shows the $K\pi^0$ invariant mass spectrum for data events from the energy region $1.5 < \sqrt{s} < 1.72$ GeV. The background contribution is estimated in the same way as for the $\chi^2(KK2\gamma)$ distribution in Sec. 6. The solid histogram in Fig. 7 represents the signal plus background distribution. The signal $K\pi^0$ mass spectrum is obtained using the simulation in the model $e^+e^- \to K^{*\pm}(892)K^\mp \to K^+K^-\pi^0$. It is seen that the $K^{*\pm}(892)K^\mp$ intermediate state is dominant in the $e^+e^- \to K^+K^-\pi^0$ reaction. The observed difference between data and simulated distributions may be due to a contribution from other intermediate states, e.g. $\phi\pi^0$, $K^{*\pm}(1410)K^\mp$, and $K_2^{*\pm}(1430)K^\mp$. Their interference with the dominant $K^*(892)K$ amplitude may lead to a shift and narrowing of the $K^*(892)$ peak in Fig. 7.

From Fig. 7 we roughly estimate that the contribution of intermediate states other than $K^*(892)\pi$ does not exceed 20%. The difference in the detection efficiency between different intermediate state is estimated comparing the efficiencies for simulated $K^*(892)K$ events and $\phi\pi^0$ events with K^+K^- invariant mass higher than 1.04 GeV/c^2. This difference does less than 20%. So, we es-

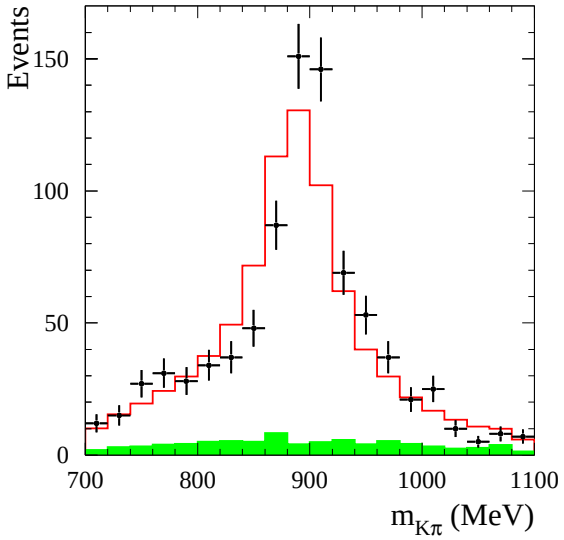


Figure 7. The $K\pi^0$ invariant mass spectrum for data events from the energy range $1.5 < \sqrt{s} < 1.72$ GeV (points with error bars). The solid histogram is the sum of the simulated $e^+e^- \to K^+K^-\pi^0$ distribution and background. The hatched histogram represents the background.

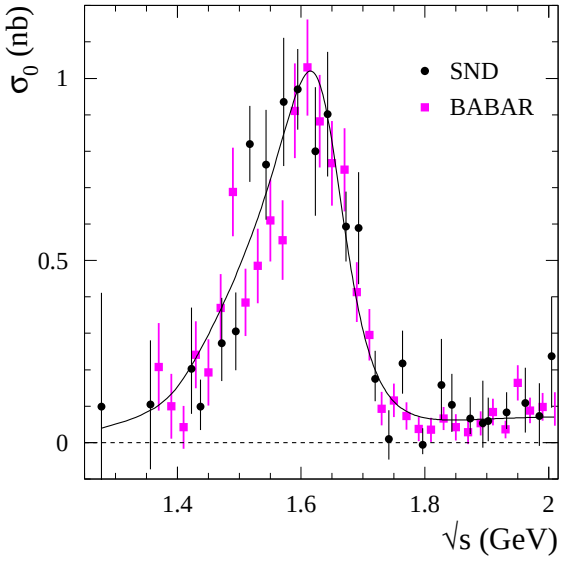


Figure 8. The $e^+e^- \to K^+K^-\pi^0$ Born cross section measured in this work (circles) compared with the BABAR [3] data (squares). The curve is the result of fit described in the text.

timate that the model uncertainty in the detection efficiency due to the contribution of non-$K^*(892)K$ intermediate states does not exceed 4%.

8 Born cross section for the process $e^+e^- \to K^+K^-\pi^0$

The formula (2) given in Sec. 6 describes the relation between the visible and Born cross sections. The experimental values of the Born cross section are determined in the following way. The measured energy dependence of the visible cross section is approximated by Eq. (2), in which the Born cross section is parametrized by some model that describes data reasonably well. As a result of the approximation, model parameters are determined and the radiation corrections are calculated as $1+\delta(s) = \sigma_{\rm vis}(s)/(\varepsilon_0(s)\sigma_0(s))$. The experimental value of the Born cross section is then determined as

$$\sigma_{0,i} = \frac{\sigma_{{\rm vis},i}}{\varepsilon_0(\sqrt{s_i})(1+\delta(s_i))}. \qquad (3)$$

In Ref. [3], the isoscalar and isovector cross sections for the process $e^+e^- \to K^*K$ were measured separately, and it was shown that the isoscalar amplitude dominates only near the maximum of the $\phi(1680)$ resonance. Below 1.55 GeV and above 1.8 GeV the isoscalar and isovector amplitudes are of the same order of magnitude. In the current analysis, a simplified two-resonance model is used to describe the $e^+e^- \to K^+K^-\pi^0$ Born cross section:

$$\sigma_0(\sqrt{s}) = \left| \frac{A_0 M_0 \Gamma_0}{M_0^2 - s - i\sqrt{s}\Gamma_0} \right.$$

$$\left. + \frac{A_1 e^{i\psi} M_1 \Gamma_1}{M_1^2 - s - i\sqrt{s}\Gamma_1} \right|^2 \frac{P(s)}{s^{3/2}}, \qquad (4)$$

where M_i and Γ_i are the masses and widths of two effective resonances, A_i are their real amplitudes, and ψ is the relative phase between the amplitudes. The function $P(s)$ describes the energy dependence of the $K^{*\pm}(892)K^{\mp}$ phase space, which takes into account the finite $K^*(892)$ width and the interference of the $K^{*+}K^-$ and $K^{*-}K^+$ amplitudes. In this model, the first term in Eq. (4) describes the total contribution of the low-lying resonances $\rho(770)$, $\omega(782)$, and $\phi(1020)$, and the excitations $\rho(1450)$ and $\omega(1420)$. The parameters M_0 and Γ_0 are taken to be equal to the mass and width of the $\phi(1020)$. The second term describes the total contribution of all excited vector resonances. Parameters A_0, A_1, M_1, Γ_1 and ψ are determined from the fit to the visible cross section data.

The values of the Born cross section calculated using Eq.(3) and the fitted curve are shown in Fig. 8. The model describes the data reasonably well: $\chi^2/{\rm ndf} = 28.2/22$, where ndf is the number of degrees of freedom ($P(\chi^2) = 16.9\%$). The fitted values of the mass and width, $M_1 = 1662 \pm 20$ MeV/c^2, $\Gamma_1 = 159 \pm 32$ MeV, are close to the Particle Data Group (PDG) values for the $\phi(1680)$ resonance [13], indicating that this resonance dominates the $e^+e^- \to K^+K^-\pi^0$ cross section.

The obtained values of the radiation correction and Born cross section are listed in Table 1. For the cross section, the statistical and energy dependent systematic uncertainties are quoted. The latter includes the systematic uncertainty in the number of $e^+e^- \to K^+K^-\pi^0$ events, and the model error of radiation correction, which is determined by varying the model parameters obtained in fit within their errors. The energy independent correlated

systematic uncertainty is 9%. It includes the systematic uncertainties in the luminosity measurement (2%) and detection efficiency (8%), and the model error of the detection efficiency (4%).

In Fig. 8, our measurement of the $e^+e^- \to K^+K^-\pi^0$ cross section is compared with the result of the most precise previous measurement by BABAR [3]. Two measurements are consistent and comparable in accuracy.

9 Study of the process $e^+e^- \to \phi\pi^0 \to K^+K^-\pi^0$

The selection criteria for $e^+e^- \to \phi\pi^0 \to K^+K^-\pi^0$ events are close to those described in Sec 3. Events with mass recoiling against the photon pair $m_{\rm rec} < 1.08$ GeV/c^2 are analyzed. The requirements on the minimum and maximum momenta of charged kaons are removed. To suppress background from the initial state radiation process $e^+e^- \to \phi(1020)\gamma \to K^+K^-\gamma$, the additional condition is imposed that the difference between the normalized energy of the most energetic photon in event $2E_{\gamma,max}/\sqrt{s}$ and $(1 - M_\phi^2/s)$ is larger than 0.1. Here M_ϕ is the $\phi(1020)$ mass.

Figure 9 shows the two-dimensional distributions of $m_{\rm rec}$ versus $m_{\gamma\gamma}$ for data events, simulated $e^+e^- \to \phi\pi^0 \to K^+K^-\pi^0$ events, and simulated events of the main background processes, $e^+e^- \to K^*K \to K^+K^-\pi^0$ and $e^+e^- \to K^+K^-(\gamma)$. Figure 10 shows the $m_{\rm rec}$ spectrum for data events with $0.1 < m_{\gamma\gamma} < 0.17$ GeV/c^2, in which the $\phi(1020)$ peak is clearly seen. The expected distribution for background events is also presented. It is seen that the simulation reproduces well both the total number of background events and the shape of the background distribution.

We define the signal ($1.00 < m_{\rm rec} < 1.04$ GeV/c^2) and sideband ($1.04 < m_{\rm rec} < 1.08$ GeV/c^2) mass regions and determine the number of $e^+e^- \to \phi\pi^0 \to K^+K^-\pi^0$ events using the equation

$$N = \frac{N_1 - k_b * N_2}{1 - k_s * k_b}, \qquad (5)$$

where N_1 and N_2 are the numbers of data events in the signal and sideband regions, respectively, k_b is the N_1/N_2 ratio for background events, and k_s is the N_2/N_1 ratio for signal events. The coefficients k_b and k_s are determined from simulation.

The detection efficiency for $e^+e^- \to \phi\pi^0 \to K^+K^-\pi^0$ events obtained using MC simulation grows from 1% at $\sqrt{s} = 1.4$ GeV to 8% at $\sqrt{s} = 1.8$ GeV, and then decreases to 6% at $\sqrt{s} = 2$ GeV.

To calculate the radiative corrections and experimental values of the Born cross section, we perform simultaneous fit to the SND data and the data from the two BABAR measurements [3,4]. The Born cross section is described by the coherent sum of the contributions of the $\rho(1450)$ and $\rho(1700)$ resonances (Model I). In this model, the masses and widths of the resonances are fixed at the PDG values [13], while the cross sections at the resonance maxima and the relative phase between the resonance amplitudes are free fit parameters. The obtained values of the Born cross section for the process $e^+e^- \to \phi\pi^0 \to K^+K^-\pi^0$ are listed in Table 2 and are shown in Fig. 11 together with the BABAR data and the fitted curve. It is seen that all three measurements are in good agreement below 1.75 GeV. In the range 1.75–2 GeV the nonstatistical spread of the measurements is observed. The fitted curve agrees with the data everywhere except in the narrow region near $\sqrt{s} = 1.58$ GeV, where excess over the curve is observed in all three measurements. The overall fit quality is unsatisfactory ($\chi^2/{\rm ndf} = 50/28$).

A better description of the data is obtained with the two resonance model, in which the mass and width of the first resonance are fixed at the PDG values for the $\rho(1700)$, and the parameters of the second resonance are free (Model II). The fit in this model yields $\chi^2/{\rm ndf} = 38/26$ ($P(\chi^2) = 6\%$), and the following parameters of the second resonance: $M = 1585 \pm 15$ MeV and $\Gamma = 75 \pm 30$ MeV. The fitted curve for Model II is also shown in Fig. 11. It should be noted that there is no a vector resonance with such parameters in the PDG table [13]. Formally, its significance calculated from the difference of the χ^2 values for Models I and II is about 3σ.

The difference in the radiation corrections calculated with Models I and II is used to estimate the model uncertainty on the Born cross section. It is 14% for the interval 1.6–1.65 GeV, 8% for the interval 1.65–1.7 GeV, and does not exceed 6% for the remaining points. The systematic uncertainty on the cross section is similar to that for the $e^+e^- \to K^+K^-\pi^0$ cross section and does not exceed 10%.

The intermediate state K^*K gives nonzero contribution to the signal region $1.00 < m_{\rm rec} < 1.04$ GeV. This leads to interference between the $\phi\pi^0$ and K^*K amplitudes, which may contribute to the measured $e^+e^- \to \phi\pi^0 \to K^+K^-\pi^0$ cross section. Using a model with a coherent sum of the $\phi\pi^0$ and K^*K amplitudes we vary the phase difference between them and study how the interference modifies the $m_{\rm rec}$ spectrum. It is found that using the procedure of the $\phi\pi^0$ signal extraction described above we actually measure a sum of the $e^+e^- \to \phi\pi^0 \to K^+K^-\pi^0$ cross section and the interference term integrated over the $m_{\rm rec}$ signal region with an uncertainty of 30%.

To understand how large the effect of the interference is, we fit the $e^+e^- \to \phi\pi^0 \to K^+K^-\pi^0$ cross section measured in this work and by BABAR [3] with the following model:

$$\begin{aligned}\sigma_{\rm meas}(s) = \sigma_{\phi\pi^0}(s) + 2\sqrt{\sigma_{\phi\pi^0}(s)\sigma_{K^*K}(s)} \\ \times \big(O_{\rm Re}(s)\cos(\psi + \psi_{K^*K} - \psi_{\phi\pi^0}) \\ + O_{\rm Im}(s)\sin(\psi + \psi_{K^*K} - \psi_{\phi\pi^0})\big), \qquad (6)\end{aligned}$$

where $\sigma_{\phi\pi^0}(s)$ and $\sigma_{K^*K}(s)$ are the cross sections corresponding to the squared moduli of the $\phi\pi^0$ and K^*K amplitudes, respectively, $\psi_{\phi\pi^0}(s)$ and $\psi_{K^*K}(s)$ are the arguments of these amplitudes, $O_{\rm Re}(s)$ and $O_{\rm Im}(s)$ are the real and imaginary parts of the specially normalized overlap integral between the $\phi\pi^0$ and K^*K amplitudes, and ψ is the relative phase between them. The functions

Table 1. The c.m. energy ($\sqrt{s}$), integrated luminosity (L), fitted number of events of $e^+e^- \to K^+K^-\pi^0$ process (N) detection efficiency (ε_0), radiation correction factor ($1+\delta$), and Born cross section for the process $e^+e^- \to K^+K^-\pi^0$ (σ_0). For the number of events, statistical and systematic errors are quoted. For the cross section, the second error is the energy-dependent uncorrelated systematic uncertainty. The energy independent correlated uncertainty on the cross section is 9%.

$\sqrt{s}$ (GeV)	L (nb^{-1})	N	ε_0	$1+\delta$	σ_0 (nb)
1.277	763	$0.7^{+2.1}_{-2.1} \pm 1.3$	0.011	0.810	$0.099^{+0.315}_{-0.311} \pm 0.189$
1.357	845	$1.5^{+2.6}_{-2.6} \pm 0.6$	0.020	0.874	$0.105^{+0.177}_{-0.178} \pm 0.043$
1.423	588	$3.4^{+2.8}_{-2.1} \pm 1.0$	0.035	0.817	$0.203^{+0.167}_{-0.124} \pm 0.061$
1.438	1505	$5.5^{+4.2}_{-3.6} \pm 1.7$	0.045	0.823	$0.098^{+0.075}_{-0.064} \pm 0.032$
1.471	619	$9.1^{+4.1}_{-3.4} \pm 0.7$	0.064	0.840	$0.273^{+0.125}_{-0.103} \pm 0.022$
1.494	754	$14.4 \pm 5.0 \pm 0.1$	0.075	0.831	$0.306 \pm 0.107 \pm 0.002$
1.517	1448	$83.2 \pm 10.6 \pm 4.3$	0.083	0.845	$0.820 \pm 0.104 \pm 0.042$
1.543	578	$33.0 \pm 6.5 \pm 0.1$	0.088	0.846	$0.763 \pm 0.151 \pm 0.003$
1.572	533	$39.0 \pm 7.3 \pm 0.7$	0.091	0.857	$0.936 \pm 0.176 \pm 0.015$
1.595	1284	$94.7 \pm 10.7 \pm 5.6$	0.087	0.873	$0.970 \pm 0.110 \pm 0.050$
1.623	545	$34.2 \pm 7.5 \pm 2.6$	0.089	0.885	$0.800 \pm 0.176 \pm 0.060$
1.643	499	$33.0 \pm 6.2 \pm 4.2$	0.081	0.907	$0.902 \pm 0.171 \pm 0.118$
1.672	1397	$59.1 \pm 9.6 \pm 2.7$	0.071	1.011	$0.593 \pm 0.096 \pm 0.032$
1.693	490	$19.2 \pm 5.0 \pm 2.3$	0.063	1.053	$0.589 \pm 0.154 \pm 0.077$
1.720	1051	$13.1^{+5.8}_{-4.6} \pm 1.5$	0.060	1.190	$0.174^{+0.078}_{-0.061} \pm 0.022$
1.742	529	$0.4^{+2.9}_{-2.1} \pm 0.6$	0.057	1.229	$0.010^{+0.079}_{-0.057} \pm 0.016$
1.764	1290	$16.0^{+6.6}_{-6.1} \pm 0.8$	0.048	1.178	$0.218^{+0.090}_{-0.083} \pm 0.003$
1.797	1424	$-0.5^{+3.5}_{-2.0} \pm 0.6$	0.052	1.054	$-0.006^{+0.045}_{-0.026} \pm 0.007$
1.826	529	$4.2^{+3.3}_{-2.6} \pm 2.2$	0.047	1.071	$0.158^{+0.126}_{-0.096} \pm 0.097$
1.844	1006	$5.1^{+4.2}_{-3.7} \pm 3.7$	0.048	1.028	$0.104^{+0.085}_{-0.074} \pm 0.084$
1.873	1606	$4.8^{+4.2}_{-3.1} \pm 0.0$	0.047	0.964	$0.066^{+0.058}_{-0.043} \pm 0.027$
1.893	624	$1.4^{+3.1}_{-1.8} \pm 0.6$	0.046	0.937	$0.053^{+0.117}_{-0.068} \pm 0.022$
1.903	1456	$3.7^{+4.0}_{-3.5} \pm 4.0$	0.045	0.956	$0.059^{+0.065}_{-0.056} \pm 0.068$
1.932	2235	$7.0^{+4.7}_{-3.8} \pm 5.8$	0.042	0.907	$0.083^{+0.056}_{-0.046} \pm 0.071$
1.962	971	$3.8^{+3.4}_{-2.8} \pm 1.5$	0.039	0.913	$0.109^{+0.097}_{-0.081} \pm 0.044$
1.985	1204	$3.2^{+4.0}_{-3.6} \pm 0.3$	0.039	0.942	$0.073^{+0.090}_{-0.083} \pm 0.069$
2.006	582	$4.9^{+3.4}_{-2.9} \pm 1.0$	0.037	0.956	$0.238^{+0.164}_{-0.142} \pm 0.047$

Table 2. The measured cross section for the process $e^+e^- \to \phi\pi^0 \to K^+K^-\pi^0$ as a function of the c.m. energy $\sqrt{s}$. The quoted errors are statistical.

$\sqrt{s}$ GeV)	σ (nb)	$\sqrt{s}$ (GeV)	σ (nb)	$\sqrt{s}$(GeV)	σ (nb)
$1.40-1.50$	$0.033^{+0.064}_{-0.020}$	$1.65-1.70$	$0.037^{+0.024}_{-0.015}$	$1.85-1.90$	$0.024^{+0.015}_{-0.009}$
$1.50-1.55$	$0.011^{+0.046}_{-0.010}$	$1.70-1.75$	$0.023^{+0.021}_{-0.013}$	$1.90-1.95$	$0.024^{+0.012}_{-0.008}$
$1.55-1.60$	$0.145^{+0.054}_{-0.040}$	$1.75-1.80$	$0.050^{+0.020}_{-0.014}$	$1.95-2.10$	$0.024^{+0.016}_{-0.009}$
$1.60-1.65$	$0.017^{+0.025}_{-0.012}$	$1.80-1.85$	$0.042^{+0.024}_{-0.014}$		

$\sigma_{K^*K}(s)$ and $\psi_{K^*K}(s)$ are determined from the fit to the $e^+e^- \to K^+K^-\pi^0$ cross section as described in Sec. 8. The $\phi\pi^0$ amplitude is parametrized using Model I introduced above. An additional fit parameter is the phase ψ. The result of the fit is shown in Fig. 12. The energy dependence of the fitted $\sigma_{\phi\pi^0}$ and interference terms are also shown.

It is seen that the interference with the K^*K amplitude gives sizable contribution to the measured $e^+e^- \to \phi\pi^0 \to K^+K^-\pi^0$ cross section listed in Table 2. Below 1.7 GeV the measured cross section cannot be directly associated with the $e^+e^- \to \phi\pi^0$ cross section.

The fitted curve in the model with interference does not differ significantly from the curve obtained in the model without interference (Model I in Fig. 11). Both models cannot reproduce the narrow structure near 1.6 GeV seen in the SND and two BABAR measurements.

The total $e^+e^- \to K^+K^-\pi^0$ cross section can be calculated by summing the cross sections listed in Tables 1 and 2. The resulting cross section accounts for the interference between the K^*K and $\phi\pi^0$ intermediate states.

10 Summary

In this paper the process $e^+e^- \to K^+K^-\pi^0$ has been studied in the c.m. energy range from 1.28 to 2 GeV. We have analyzed the data with an integrated luminosity 26.4 pb^{-1} accumulated in the experiment with the SND detector at the VEPP-2000 e^+e^- collider in 2011-2012. It has been shown that the process $e^+e^- \to K^+K^-\pi^0$ in the energy range under study proceeds predominantly through the $K^*(892)^\pm K^\mp$ intermediate state. The signal from the intermediate state $\phi\pi^0$ has been also observed.

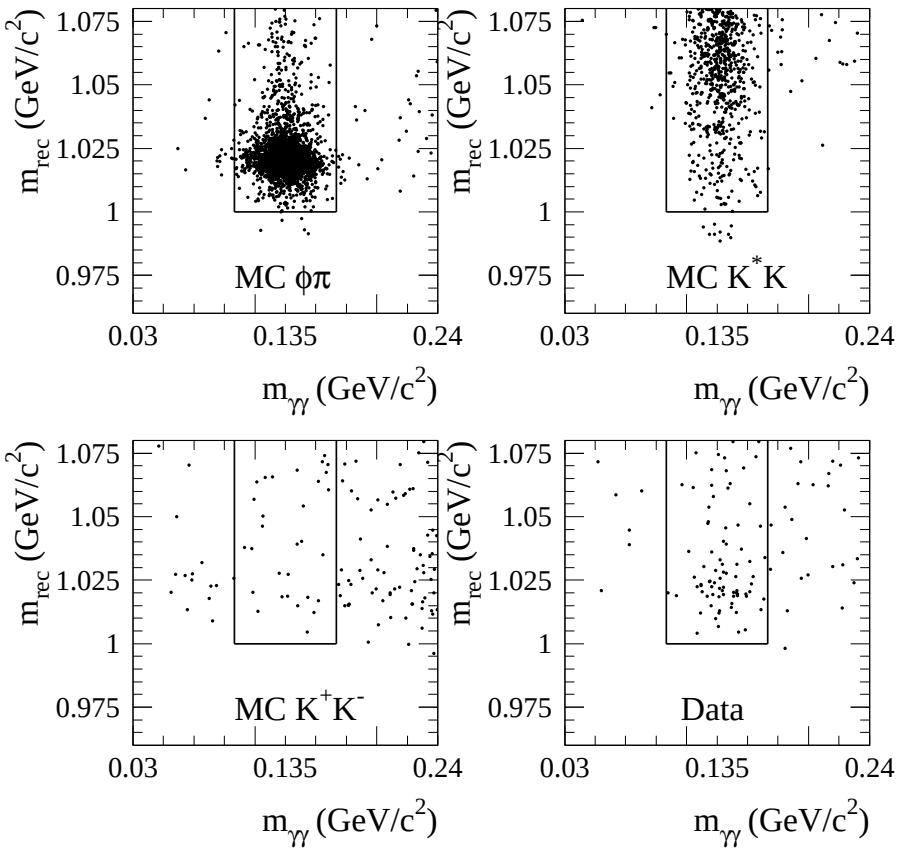


Figure 9. The two-dimensional $m_{\rm rec}$ versus $m_{\gamma\gamma}$ distribution for selected data and simulated events of the processes $e^+e^- \to \phi\pi^0 \to K^+K^-\pi^0$, $e^+e^- \to K^*K \to K^+K^-\pi^0$, $e^+e^- \to K^+K^-(\gamma)$. The lines indicate the region of invariant masses ($1.00 < m_{\rm rec} < 1.08$ GeV/c^2, $0.1 < m_{\gamma\gamma} < 0.17$ GeV/c^2) used in the $e^+e^- \to \phi\pi^0$ analysis.

The cross sections for the process $e^+e^- \to K^+K^-\pi^0$ (without $\phi\pi^0$) and $e^+e^- \to \phi\pi^0 \to K^+K^-\pi^0$ have been measured separately. They agree well with the previous measurements in the BABAR experiment and have comparable accuracy.

For the process $e^+e^- \to \phi\pi^0 \to K^+K^-\pi^0$ we have studied the effect of the interference between the $\phi\pi^0$ and K^*K amplitudes. It has been found that the interference gives sizable contribution (up to 100%) to the measured $e^+e^- \to \phi\pi^0 \to K^+K^-\pi^0$ cross section below 1.7 GeV. In this region we actually measure the sum of the $\phi\pi^0$ cross section and the interference term with the model uncertainty of 30%. Within this uncertainty, the total $e^+e^- \to K^+K^-\pi^0$ cross section calculated as a sum of the two measured cross sections accounts correctly for the interference between the $\phi\pi^0$ and K^*K amplitudes.

In the narrow region near $\sqrt{s} = 1.58$ GeV all three existing measurements of the $e^+e^- \to \phi\pi^0$ cross section, performed by SND (this work) and BABAR [3,4]), show excess over the model including known vector resonances. This excess can be interpreted as a contribution of the resonance with $M = 1585\pm15$ MeV and $\Gamma = 75\pm30$ MeV. Its significance is estimated to be about 3σ.

The work was performed using the unique scientific facility "Complex VEPP-4 – VEPP-2000".

References

1. A. Romanov et al., in Proceedings of PAC 2013, Pasadena, CA USA, p.14.
2. D. Bisello *et al.*, Z. Phys. C **52**, 227 (1991).
3. B. Aubert *et al.* (BABAR Collaboration), Phys. Rev. D **77**, 092002 (2008).
4. J. P. Lees *et al.* (BABAR Collaboration), Phys. Rev. D **95**, 052001 (2017).
5. M. N. Achasov et al. Nucl. Instrum. Methods Phys. Res., Sect. A 598, 31 (2009); V. M. Aulchenko et al., ibid. 598, 102 (2009); A. Yu. Barnyakov et al., ibid. 598, 163 (2009); V. M. Aulchenko et al., ibid. 598, 340 (2009).
6. A. Y. Barnyakov *et al.*, JINST **9**, C09023 (2014); A. Y. Barnyakov *et al.*, Instrum. Exp. Tech. **58**, 30 (2015).

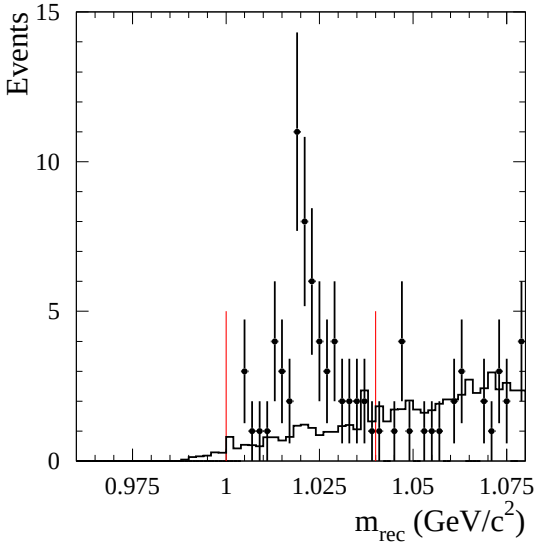


Figure 10. The m_{rec} distributions for data events (points with error bars). The histogram represents a sum of the simulated distributions for $e^+e^- \to K^*K \to K^+K^-\pi^0$ events and events of the background processes (1). The vertical lines indicate the region $1.00 < m_{\rm rec} < 1.04$ GeV/c^2 used for measurement of the $e^+e^- \to \phi\pi^0 \to K^+K^-\pi^0$ cross section.

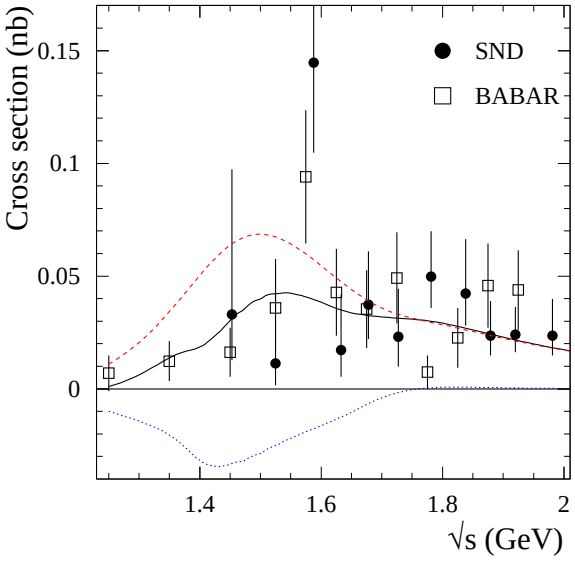


Figure 12. The cross section of the process $e^+e^- \to \phi\pi^0 \to K^+K^-\pi^0$ obtained in this work and in the BABAR experiment [3]. The solid curve is the result of the fit to the cross section data with Eq. (6). The dashed and dotted curves represent the $\sigma_{\phi\pi^0}$ term and the interference terms of Eq. (6), respectively.

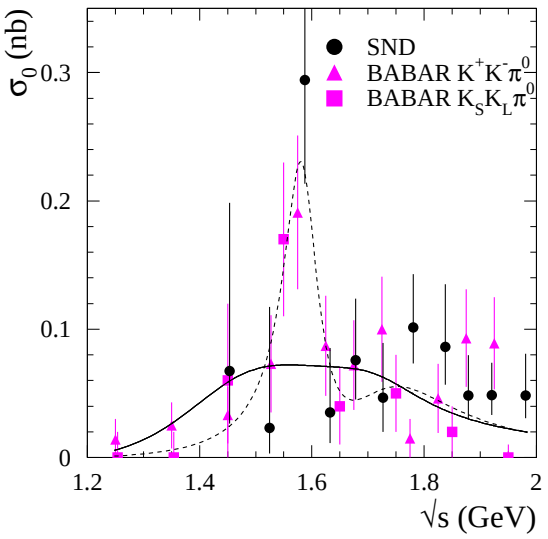


Figure 11. The cross section for the process $e^+e^- \to \phi\pi^0 \to K^+K^-\pi^0$ obtained in this experiment in comparison with the two BABAR measurements [3,4]. The solid and dashed curves represent the results of the fit in Models I and II, respectively.

7. E. A. Kuraev, Z. K. Silagadze, Phys. Atom. Nucl. **58**, 1589 (1995).
8. E. A. Kuraev and V. S. Fadin, Sov. J. Nucl. Phys. **41**, 466 (1985) [Yad. Fiz. **41**, 733 (1985)].
9. G. Bonneau and F. Martin, Nucl. Phys. B **27**, 381 (1971).
10. S. Agostinelli *et al.* (GEANT4 Collaboration), Nucl. Instrum. Methods Phys. Res., Sect. A **506**, 250 (2003).
11. V. M. Aulchenko *et al.* (SND Collaboration), Phys. Rev. D **91**, 052013 (2015).
12. M. N. Achasov *et al.* (SND Collaboration), Phys. Rev. D **94**, 112006 (2016).
13. P. A. Zyla *et al.* (Particle Data Group), Prog. Theor. Exp. Phys. **2020**, 083C01 (2020).